Journal of Solid State Chemistry 184 (2011) 2420–2427

Contents lists available at ScienceDirect

Journal of Solid State Chemistry

journal homepage: www.elsevier.com/locate/jssc

Stepwise synthesis, characterization, and electrochemical properties of ordered mesoporous carbons containing well-dispersed Pt nanoparticles using a functionalized template route

Shou-Heng Liu *, Shih-Che Chen

Department of Chemical and Materials Engineering, National Kaohsiung University of Applied Sciences, Kaohsiung 80778, Taiwan

ARTICLE INFO

Article history:
Received 31 August 2010
Received in revised form
5 July 2011
Accepted 11 July 2011
Available online 19 July 2011

Keywords:
Platinum
Ordered mesoporous carbons
Functionalization
Electrocatalysts
Oxygen reduction reaction

ABSTRACT

A stepwise method is described for the accurately controlled growth of Pt nanoparticles supported on ordered mesoporous carbons (Pt–OMC) by the nanocasting of carbon and metal precursors in the pore channels of mesoporous silicas functionalized with Si–H groups. Results obtained from N_2 adsorption/desorption isotherms and transmission electron microscopy showed well-dispersed Pt nanoparticles (2–3 nm) on Pt–OMC with high surface area (837 $m^2\,g^{-1}$) and regular pore channels (2.9 nm), which facilitate reactant/product diffusion. X-ray diffraction and X-ray photoelectron spectroscopy indicated that Pt nanoparticles in the Pt–OMC sample were mostly present in the metallic form of a face-centered cubic (fcc) crystalline structure. The Pt–OMC catalyst was found to have superior electrocatalytic properties during oxygen reduction reaction as compared to typical commercial electrocatalysts.

1. Introduction

Fuel cells have been recognized as one of next-generation electrical power sources for light-duty vehicles and stationary or portable applications as an alternative to conventional power sources [1–3], for instance, internal combustion engines and secondary batteries [4,5]. In the past few years, much effort from government, industry, and academy has been devoted to develop polymer electrolyte membrane fuel cells (PEMFCs)/direct methanol fuel cells (DMFCs) and great advances have been achieved; however, two major remaining challenges to widespread use, namely cost and lifetime, make PEMFCs/DMFCs far from market launch [4,6]. In terms of the former, upward pressure on price of Pt that is the active species in the most of the presently used electrocatalysts requires a decrease in the usage of Pt and/or increase in the mass specific activity of the active species [7]. Thus, support materials with high surface area favorable to Pt dispersion, proper textural properties helpful to kinetics of both anode and cathode reactions, and high electronic conductivity are highly desirable [8,9]. With respect to the latter, structural stability of supports during the operational conditions, the interaction between the active species and supports [10–15] (for example, the surface properties of supports and/or Pt loading method capable of stabilizing Pt nanoparticles) are necessary to maintain electrocatalytic activity under long-term operations. As such, structural and surface properties of support materials and loading method of Pt nanoparticles would play crucial roles in fabrication of cost-down Pt-containing electrocatalysts with high and long-term electrocatalytic activity.

Nanostructured carbon materials that possess high surface area, tailorable textural structure, good electronic conductivity, and corrosion resistance are ideal supports for Pt-containing electrocatalysts [5,16–19]. Indeed, apart from the standard commercial support (Vulcan XC-72) used in electrocatalysts for PEMFCs/DMFCs, carbon nanotubes, carbon nanofibers, and mesoporous carbons have been shown to be pertinent support materials for fabricating efficient anodic/cathodic electrocatalysts [2,20–24]. However, it is well-known that the properties of the incorporated Pt metals depend strongly on their particle size, shape, and dispersion. Conventional techniques for embedding platinum or mix-metal nanoparticles in the porous supports typically invoke post-synthesis treatments, such as impregnation [25–29], adsorption [30,31], ion-exchange [32–34] and colloidal or microemulsion [35–40]. Nevertheless, owing to their chemically inert nature, most nanostructured carbon materials normally have a lack of desirable functional groups on their surfaces and hence the uncontrolled growth of Pt nanoparticles supported on these supports are vulnerable to aggregation during the synthetic process and electrocatalytic reactions, due to weak interaction between metal particles and supports, which shorten

* Corresponding author. Fax: +886 7 3830674.
E-mail address: shliu@kuas.edu.tw (S.-H. Liu).

0022-4596/$ - see front matter © 2011 Elsevier Inc. All rights reserved.
doi:10.1016/j.jssc.2011.07.016

whole lifetime of PEMFCs/DMFCs. Also, the colloidal method is complex and time-consuming, and tends to result in undesirable loss of the noble metals.

In this paper, we report on a novel procedure, based on the pyrolysis of carbon and Pt precursors in a functionalized SBA-15 mesoporous silica, which was prepared by a stepwise method, to fabricate a well-dispersed and accurately controlled Pt nanoparticles supported on ordered mesoporous carbons (Pt–OMC). Characterization of Pt–OMC sample was investigated by a variety of analytical and spectroscopic techniques, such as X-ray diffraction (XRD), N_2 adsorption/desorption, transmission electron microscopy (TEM), and X-ray photoelectron spectra (XPS). These Pt–OMC samples so fabricated were examined as electrocatalysts for oxygen reduction reaction (ORR) at cathode by electrochemical techniques, aiming to improve the electrocatalytic activity.

2. Experimental

2.1. Catalyst preparation

Firstly, SBA-15 mesoporous silica was synthesized according to the procedure reported by Zhao et al. [41]. Briefly, 2.9 g of neutral tri-block co-polymer surfactant (Pluronic 123; $EO_{20}PO_{70}EO_{20}$, MW=5800, Aldrich) was dissolved in a mixture of 37% HCl solution (12.2 g) and water (84.7 g) at room temperature. After adding tetraethyl orthosilicate (TEOS; 98%, Acros), the resultant mixture was stirred at 313 K for 20 h and then transferred into a polypropylene bottle and reacted at 373 K under static condition for 24 h. The solid products were recovered by filtration and dried at room temperature overnight to obtain as-synthesized SBA-15 (denoted as SBA-15as). Secondly, ca. 3 g of SBA-15as was dispersed in 100 mL of dry toluene at 353 K under N_2 flux, followed by adding 20 mL of trimethylchlorosilane (TMCS; 98%, Acros) dropwise and stirring for 20 h. The mixture was filtered with toluene and then dried at 353 K under vacuum. The surfactant template was removed by ethanol extraction. Modified SBA-15 with Si–CH_3 groups (denoted as SBA–15CH_3) on the external surface was obtained. Thirdly, ca. 2 g of SBA–15CH_3 was dehydrated at 373 K for at least 6 h in vacuum, dispersed in toluene and then adding 15 mL of thionyl chloride (99.7%, Acros) into the mixture, which was stirred at 353 K for 24 h in the N_2 atomosphere. The product was filtered with toluene and dried again in vacuum at 353 K. About 0.25 g of lithium aluminum hydride ($LiAlH_4$; 98%, Acros) was dissolved in 100 mL of dry tetrahydrofuran (THF; 99.6%, Acros) under flowing N_2, then added into the above solid powder and the mixture was stirred for 36 h. The resultant solid was washed with THF repeatedly to obtain SBA–15H sample. Fourthly, ca. 1 g of SBA–15H sample was outgassed at room temperature and dispersed in absolute ethanol solution, followed by adding a certain amount of hexachloroplatinic acid (H_2PtCl_6; 39%, Acros) into the mixture. About 20 mL of dichloromethane (99%, Acros) was added to introduce more Pt precursors into the pore channels of SBA–15H. The resultant sample, which is denoted as Pt–SBA-15 was dried under vacuum at room temperature. Finally, subsequent replication of Pt–SBA-15 into Pt–OMC was carried out using the modified procedures described earlier [42,43]. Typically, ca. 0.5 g of Pt–SBA-15 was dehydrated at 333 K for 12 h under vacuum. Oxalic acid (98%, Acros) was used as the acid catalyst for polymerization of furfuryl alcohol (FA, 98%, Acros) solution, which was infiltrated in Pt–SBA-15 by incipient wetness impregnation at room temperature, followed by polymerization at 333 K then at 353 K each for 12 h in air. The resultant composite was ramped to 1073 K with a heating rate of 1 K min^{-1} and maintained at that temperature for 3 h under vacuum. The resultant black powders (denoted as Pt–OMC-as) were leached with HF (1 wt%) aqueous solution for at least 24 h to remove the silica template, washed with distilled water and alcohol, then dried at 373 K to obtain the Pt–OMC sample.

2.2. Physicochemical characterizations

X-ray diffraction (XRD) patterns of all samples were recorded on a PANalytical (X'Pert PRO) instrument using Cu-$K\alpha$ radiation (λ=0.1541 nm). Fourier transform infrared (FTIR) spectra were collected on a Bio-rad 165 spectrometer with 4 cm^{-1} resolution using KBr pellets at room temperature. The concentrations of platinum in various samples were analyzed by flame atomic absorption (AA, Hitachi Z-8200) spectroscopy. X-ray photoelectron spectra (XPS) were acquired through an energy analyzer with a constant pass energy of 20 eV followed by irradiating a sample pellet (6 mm in diameter) with a monochromatic Al-$K\alpha$ (1486.6 eV) X-ray under ultra-high vacuum condition (10^{-10} Torr). Nitrogen adsorption isotherms were measured at 77 K on a Micromeritics ASAP 2010 analyzer. Pore size distribution curves were calculated by the BJH method from the adsorption branch. The BET specific surface area was calculated from nitrogen adsorption data in the relative pressure (P/P_0) range from 0.05 to 0.2. The total pore volume was estimated from the amount adsorbed at the P/P_0 of 0.99. For transmission electron microscopy (TEM, JEOL JEM-2100 F) experiments, samples were first suspended in acetone (99.9 vol%) by ultrasonication, followed by deposition of the suspension on a lacey carbon grid. The high-resolution TEM images were obtained at room temperature using an electron microscope that has a field-emission gun at an acceleration voltage of 200 kV.

2.3. Electrochemical measurements

The electrocatalytic measurements were performed in a single compartment glass cell with a standard three-electrode configuration. A glassy carbon electrode with a diameter of 5 mm was used as a working electrode and a saturated Ag/AgCl electrode and a platinum wire were used as reference and counter electrodes, respectively. The glassy carbon thin-film electrode was prepared according to the method reported earlier [44]. Typically, ca. 5 mg of sample was added into 2.5 mL deionized water, followed by ultrasonication treatment for 0.5 h. Then, ca. 20 μL of the resultant suspension mixture was withdrawn and injected onto the glassy carbon electrode, followed by drying in air at 333 K for 1 h. Finally, 20 μL of 1% Nafion® (DuPont) solution was added as a binder under N_2 environment. Electrocatalytic activity measurements of Pt–OMC and a commercial Johnson–Matthey Pt/C sample (20 wt% Pt on Vulcan XC-72, denoted as JM–Pt/C) were performed on a galvanostat/potentiostat (CHI Instruments, 727D). ORR was evaluated by a linear sweep voltammetry (LSV) technique. The 0.1 M H_2SO_4 electrolyte was saturated with ultrahigh purity oxygen for at least 0.5 h. The polarization curves were obtained between 0 and 0.8 V at a scanning rate of 5 mV s^{-1} and a rotating speed of 1600 rpm under room temperature condition.

3. Results and discussion

The physicochemical properties of the functionalized SBA-15 samples were verified by a variety of different spectroscopic and analytical techniques. As displayed in Fig. 1a, the small-angle XRD patterns of SBA–15CH_3 and SBA–15H samples all reveal one intense (1 0 0) diffraction peak and two weak diffraction peaks of (1 1 0) and (2 0 0), indicating the existence of a well-ordered hexagonal array of mesopores with two-dimensional (2-D) channel structure even after the functionalization treatment of as-synthesized SBA-15 [45]. Furthermore, the unit cell parameter (a, Table 1) observed for SBA–15H remains practically intact

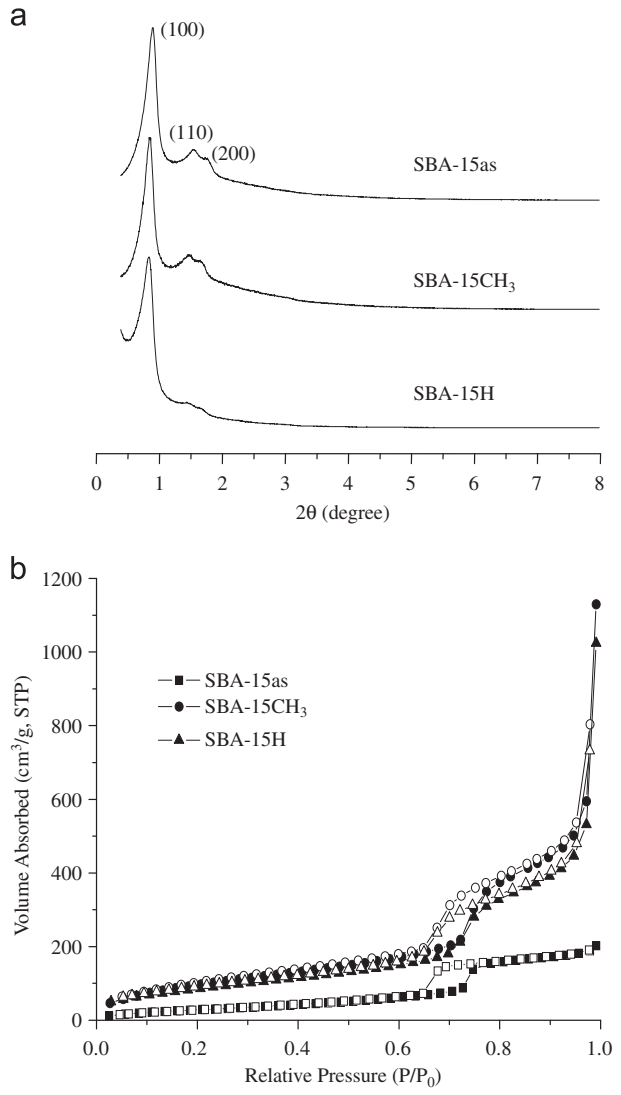

Fig. 1. (a) Small-angle powdered XRD patterns and (b) N_2 adsorption/desorption isotherms of SBA-15as, SBA–15CH_3 and SBA–15H.

Table 1
Physical properties of SBA–15as, SBA–15CH_3 and SBA–15H obtained from N_2 adsorption/desorption measurements at 77 K.

Sample	a[a] (nm)	S_{BET}[b] (m^2g^{-1})	D_{BJH}[c] (nm)	V_{tot}[d] ($cm^3\,g^{-1}$)	$W_{thickness}$[e] (nm)
SBA–15as	11.5	118	–	0.3	–
SBA–15CH_3	11.6	837	8.1	1.1	3.5
SBA–15H	11.6	820	8.1	1.0	3.5

[a] Unit cell parameter.
[b] BET surface area.
[c] BJH pore diameter.
[d] Total pore volume.
[e] Wall thicknesses were calculated as: $a - D_{BJH}$.

during functionalization process. All N_2 adsorption/desorption curves obtained from SBA–15as, SBA–15CH_3 and SBA-15H samples show the typical type-IV isotherm with a well defined hysteresis loop at a relative pressure P/P_0 of 0.6–0.8 (Fig. 1b). As a result, the BET surface area, pore volume, and pore size distribution (by BJH method) of various samples are summarized in Table 1. The SBA–15H samples have high surface areas (820 m^2/g) and uniform pore size distributions (8.1 nm). This result is consistent with the XRD patterns, which indicate that the parent mesoporous structure was still retained during the modification process. FTIR spectra of the SBA–15CH_3 and SBA–15H are shown in Fig. 2. The existence of feature peaks at 2900–3000 and 830 cm^{-1} were assigned to C–H and Si–C bonding, respectively, indicating that Si–CH_3 has been modified on the external surface of SBA-15 after the as-synthesized SBA-15 was treated with TMCS. It is noted that the inner surface of mesopores was not disturbed because the surfactant molecules still occupy the pores of SBA-15. A band at ca. 960 cm^{-1}, which is attributed to the Si–O stretching of the Si–OH groups, was observed for SBA–15CH_3 samples due to the extraction of the surfactant by ethanol solution. The vanishing of the peak at 960 cm^{-1} and formation of two new peaks at ca. 2240 and 860 cm^{-1} assigned due to Si–H stretching and bending vibrations, respectively, were evident for SBA–15H samples. This implied the creation of Si–H in the inner pore surface of SBA–15H. Based on the above combined results from various characterization techniques (XRD, N_2 adsorption/desorption isotherms, and FTIR), it is indicative that the SBA–15H samples possess regular mesoporous channels, high surface area and uniformly functionalized layer of Si–H groups, which would be desirable as hard templates for the accurate control of Pt nanoparticles on ordered mesoporous carbons during nanocasting process.

As described in Section 2, the reduction reaction between Si–H and H_2PtCl_6 may occur as below upon incorporating the Pt precursors into the pores of SBA–15H samples.

$$6{\equiv}SiH + H_2PtCl_6 \rightarrow 6{\equiv}SiCl + Pt + 4H_2$$

$\equiv$SiCl is unstable in air and reacts with H_2O to form $\equiv$SiOH, which is proved by the FTIR spectrum in Fig. 2c as shown in the following reaction:

$$\equiv SiCl + H_2O \rightarrow \equiv SiOH + HCl$$

The surface area, pore diameter, and pore volume of Pt–SBA-15 samples shown in Table 2 are smaller than those of SBA–15H (Table 1), which can be ascribed to the incorporation of Pt. As

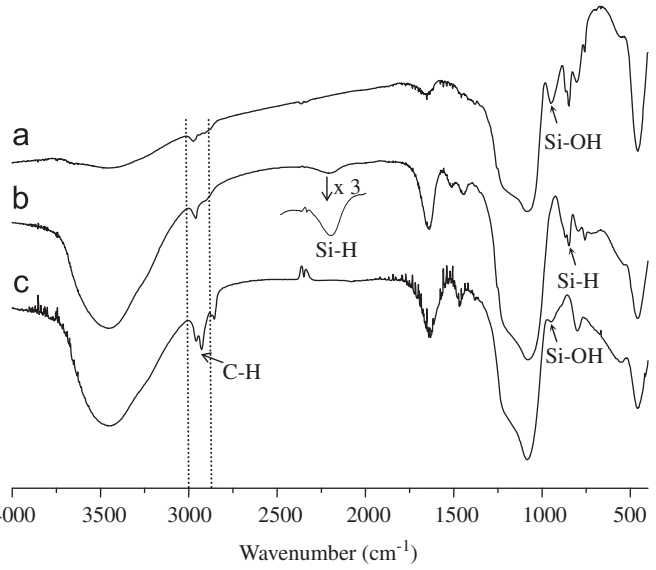

Fig. 2. FTIR spectra of (a) SBA–15CH_3, (b) SBA–15H and (c) Pt–SBA-15 samples.

shown in Fig. 3a, the remarkable decrease of main diffraction peak (1 0 0) in Pt–SBA-15 samples was also observed upon the incorporation of Pt precursors, revealing that the size and density of the Pt particles have considerable influence on the structure of the silica template [46,47]. Likewise, the diffraction feature cannot be obviously found after infiltration and carbonization of carbon precursors in Pt–OMC-as samples. However, the mesostructure of Pt–OMC was observed because they arise from the skeleton of the SBA-15 mesoporous silica template, which was subsequently removed by acid washing after carbonization. The N_2 adsorption/desorption curve and their corresponding pore size distribution of Pt–OMC samples are shown in Fig. 4, indicating the typical type-IV isotherm with a well defined hysteresis loop and narrow mesoporosity. Accordingly, the high BET surface area, pore volume, and uniform pore size distribution of Pt–OMC samples (Table 2) can be found to be 837 $m^2\ g^{-1}$, 1.1 $cm^3\ g^{-1}$ and 2.9 nm, respectively. In Fig. 3b, the large-angle XRD patterns of various samples show distinct (1 1 1), (2 0 0), (2 2 0), and (3 1 1) diffraction peaks at $2\theta = 39.8^\circ$, 46.2°, 67.8°, and 81.3°, respectively, in accordance with those of Pt metal particle with a face-centered cubic (fcc) structure regardless of their textural diversity. Based on the Scherrer formula [48,49], the average sizes of Pt deduced from (2 2 0) peak of the XRD profiles in Pt–SBA-15 and Pt–OMC were found to be 1.6 and 2.5 nm, respectively, suggesting that Pt particles were slightly aggregated during carbonization process.

The structure and metal dispersion of Pt–OMC samples were further verified by TEM measurements. As shown in Fig. 5a, TEM image of Pt–OMC exhibit a uniform array of mesopores with a long-range order. It can be seen that an average particle size of ca. 2–3 nm Pt is uniformly dispersed on the surface of the carbon rods in the Pt–OMC (Fig. 5b), which is in accordance with the aforementioned XRD results. This indicates that the mesostructures of

Table 2
Textural properties of Pt–SBA-15, Pt–OMC-as and Pt–OMC obtained from N_2 adsorption/desorption measurements at 77 K.

Sample	Pt (wt%)	a[a] (nm)	S_{BET}[b] (m^2g^{-1})	D_{BJH}[c] (nm)	V_{tot}[d] (cm^3g^{-1})	$W_{thickness}$[e] (nm)
Pt–SBA-15	15.1	–	377	7.7	0.6	–
Pt–OMC-as	14.6	–	152	–	0.3	–
Pt–OMC	13.5	10.4	837	2.9	1.1	7.5

[a] Unit cell parameter.
[b] BET surface area.
[c] BJH pore diameter.
[d] Total pore volume.
[e] Wall thicknesses were calculated as: a -D_{BJH}.

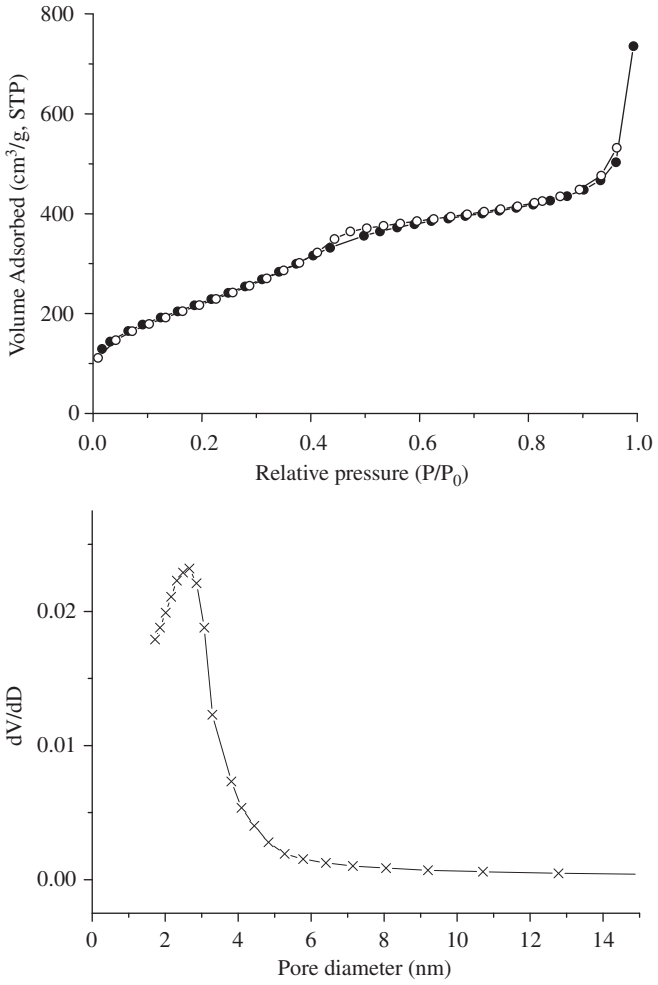

Fig. 4. N_2 adsorption/desorption isotherm (top) and corresponding pore size distribution (bottom) of Pt–OMC samples.

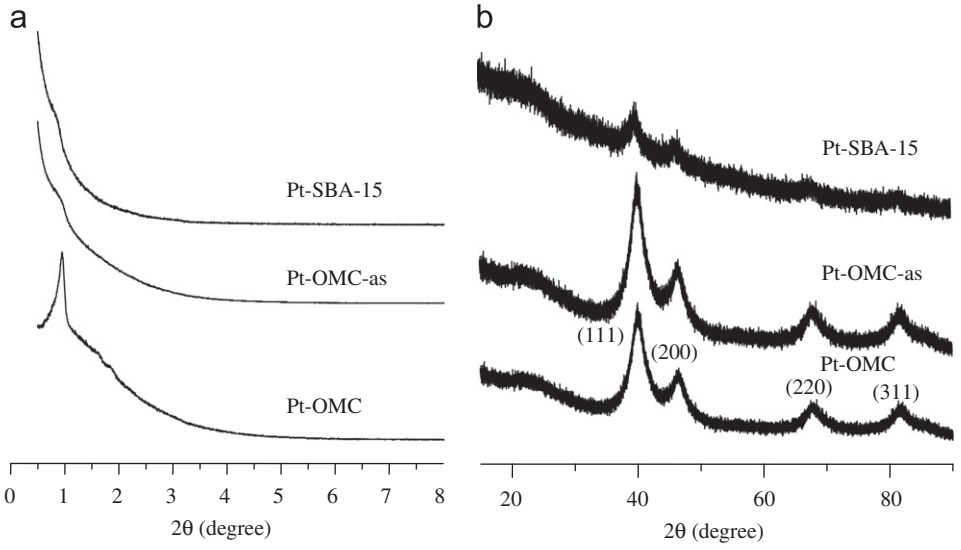

Fig. 3. (a) Small- and (b) large-angle powdered XRD patterns of Pt–SBA-15, Pt–OMC-as and Pt–OMC samples.

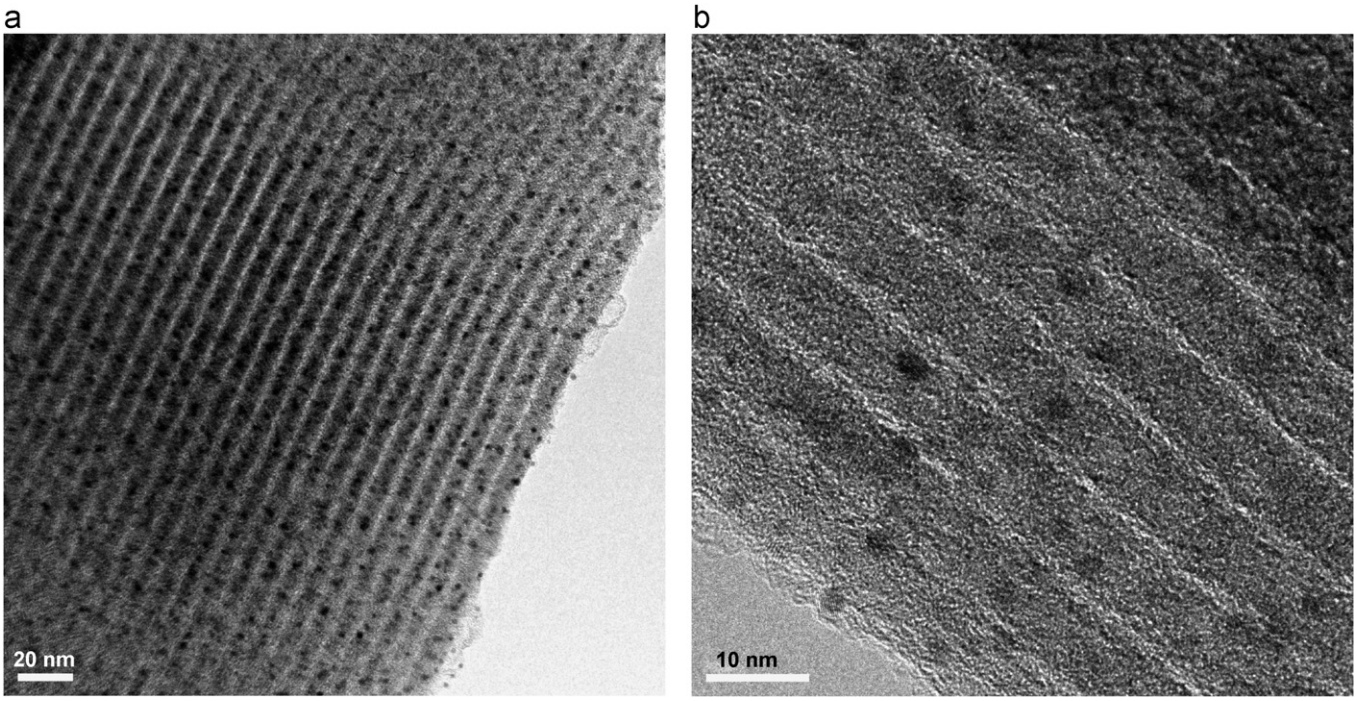

Fig. 5. (a) TEM and (b) high resolution TEM images of Pt–OMC samples.

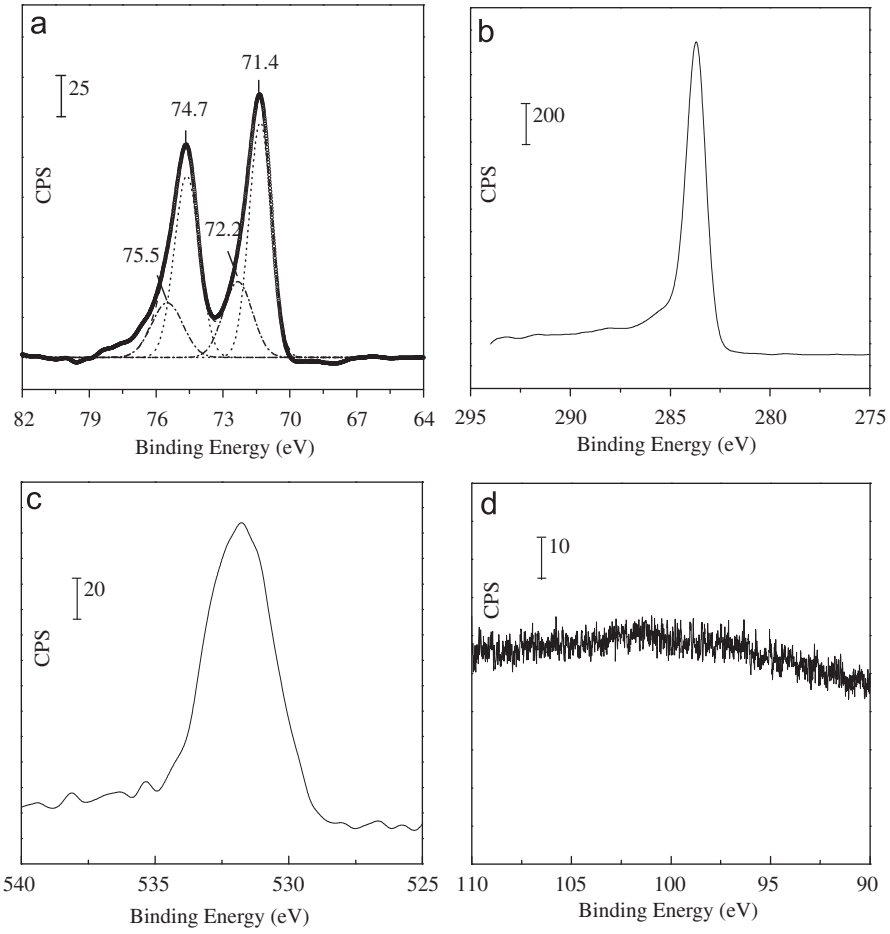

Fig. 6. XPS spectra of Pt–OMC samples at (a) Pt 4*f*, (b) C 1*s*, (c) O 1*s* and (d) Si 2*p* regions.

SBA–15H samples facilitate a confined effect for the Pt nanoparticles, most likely due to the restricted Ostwald ripening and/or migration-coalescence of Pt particles in these structures

XPS spectroscopy was also used to characterize the nature of platinum, carbon, and oxygen species, as exemplified by the results obtained from the Pt–OMC sample in Fig. 6. Accordingly, the Pt XPS spectrum in Fig. 6a could be deconvoluted into two pairs of doublets with the intense peaks centered at binding energies of 71.4 and 74.7 eV, respectively. These two peaks are attributed to Pt $4f_{7/2}$ and Pt $4f_{5/2}$ excitations of metallic platinum, whereas the other weaker peaks at 72.2 and 75.5 eV are due to oxidized platinum. Thus, it is indicative that a substantial amount of H_2PtCl_6 was reduced to metallic Pt(0) by highly reducing bonds (Si–H) of SBA–15H. On the other hand, the C 1*s* XPS spectrum of the Pt–OMC sample in Fig. 6b consists of a peak at ca. 284.5 eV, which can be ascribed due to the sp^2 graphitic carbon species. The

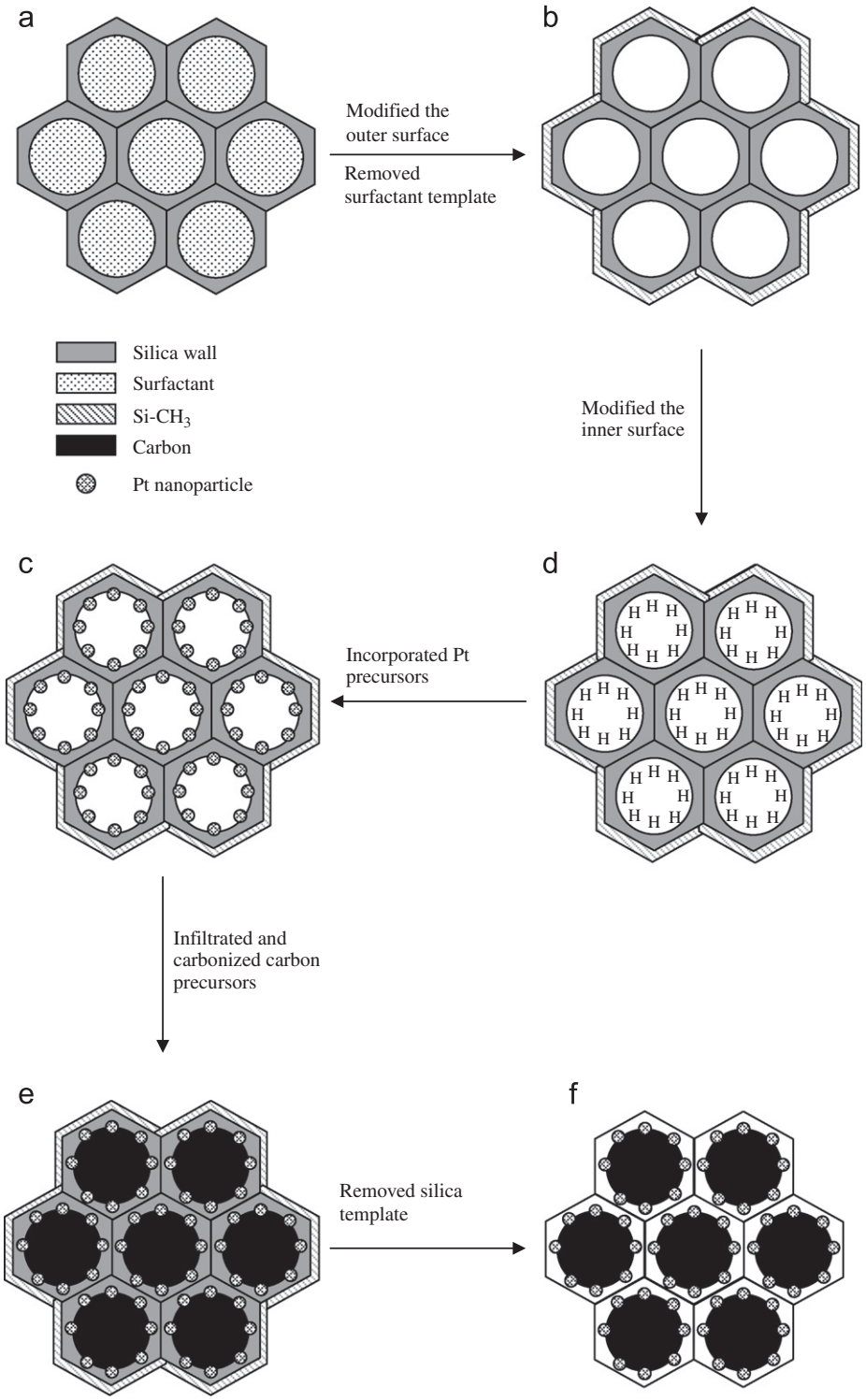

Fig. 7. Schematic illustrations of synthesis procedure for Pt–OMC samples: (a) SBA–15as; (b) SBA–15CH_3; (c) SBA–15H; (d) Pt–SBA-15; (e) Pt–OMC-as; and (f) Pt–OMC.

full width at half-maximum (FWHM) of graphite peak is ca. 1.2 eV observed in the C 1*s* spectrum for Pt–OMC sample, suggesting the presence of less ordered graphene layers compared to graphitized carbon black (0.82 eV) [50–52]. Again, this may be attributed to perturbation of the deposited Pt nanoparticles along the carbon rods of ordered mesoporous carbons. Likewise, the O 1*s* spectra (Fig. 6c) show single broad peaks, indicating the existence of various oxygen species in the Pt–OMC sample. Additional XPS experiments revealed no detectable traces of Si in the Pt–OMC samples (Fig. 6d), suggesting that silica templates have been completely eliminated by HF solution.

Based on the above-findings, the overall synthesis scheme for the formation of Pt–OMC may be summarized as illustrated in Fig. 7. Firstly, as-synthesized SBA-15 (Fig. 7a) was modified with $Si–CH_3$ groups on the outer surface, followed by removal of surfactant template with solvent extraction. Secondly, the inner surface of SBA–15CH_3 (Fig. 7b) was modified with a homogeneous layer of Si–H groups on the silica walls. Thirdly, introducing Pt precursors ($PtCl_6^{-}$) into the channels of SBA–15H (Fig. 7c) to obtain Pt–SBA-15 (Fig. 7d) in which oxidized Pt was reduced by the Si–H groups homogeneously dispersed on the pore surface. Finally, the Pt–SBA-15 was infiltrated with carbon precursors, then subjected to carbonization at 1073 K under vacuum (Fig. 6e), followed by removal of the silica template with hydrofluoric acid solution, washing, and drying to obtain the final Pt–OMC product (Fig. 7f).

To preliminarily evaluate the electrocatalytic activities of Pt–OMC and the commercially available JM–Pt/C (John–Matthey; 20 wt% Pt on Vulcan XC-72) catalysts during ORR, additional LSV tests in a regular electrochemical cell were performed. Fig. 8 shows polarization curves of JM–Pt/C and Pt–OMC samples in 0.1 M H_2SO_4 solution saturated with oxygen at a scan rate of 5 mV s^{-1} and a rotating speed of 1600 rpm. The polarization curves have two characteristic regions, including a well-defined limiting-current region (0–0.4 V vs. Ag/AgCl) and a mixed diffusion-kinetic control region (0.4–0.8 V vs. Ag/AgCl). It was found that the ORR of Pt–OMC catalyst occurs at higher potential (0.75 V vs. Ag/AgCl) and the stable reduction current is larger than that of JM–Pt/C catalyst, which indicates that well-dispersed and controlled size of Pt nanoparticles can improve the ORR activity. It should be noted that, unlike JM–Pt/C, the Pt–OMC catalyst contains only ca. 13.5 wt% of Pt. In terms of the production cost and the mass activity of the Pt catalyst, Pt–OMC catalysts are superior than JM–Pt/C. Thus, the supported Pt–OMC exhibited surpassing activity during ORR in comparison with JM–Pt/C and hence should render future practical and cost-effective applications for PEMFCs and DMFCs.

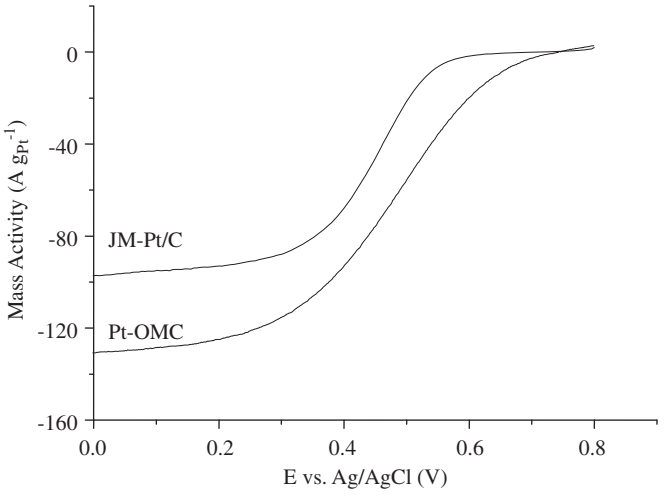

Fig. 8. Polarization curves of JM–Pt/C and Pt–OMC catalysts in 0.1 M H_2SO_4 solution saturated with oxygen at a scan rate of 5 mV s^{-1} and a rotating speed of 1600 rpm.

4. Conclusion

In summary, the novel Pt–OMC catalysts for ORR reported herein were fabricated by the nanocasting of carbon and metal precursors in the pore channels of mesoporous silicas via a stepwise functionalization possess. Combined the data from N_2 adsorption/desorption isotherms and TEM revealing that well-dispersed Pt nanoparticles (2–3 nm) on ordered mesoporous carbon with high surface area and regular pore channels, which facilitate reactant/product diffusion. Further studies by XRD and XPS indicated that 13.5 wt% of Pt nanoparticles presented on the carbon rods of Pt–OMC catalysts were the metallic Pt(0) with a face-centered cubic (fcc) crystalline structure. Furthermore, the Pt–OMC catalysts were found to have superior electrocatalytic properties compared to common commercial catalysts during ORR. Thus, the supported Pt–OMC catalysts so fabricated should render future practical and cost-effective applications in hydrogen-energy related areas, for example, as electrocatalysts for DMFCs and PEMFCs.

Acknowledgment

The financial support of the Taiwan National Science Council (NSC 99-2221-E-151-044-MY2 and 99-2221-E-151-023-MY2) is gratefully acknowledged.

References

[1] X.D. Xue, L. Gu, X.B. Cao, Y.Y. Song, L.W. Zhu, P. Chen, J. Solid State Chem. 182 (2009) 2912.
[2] R.F. Service, Science 324 (2009) 1257.
[3] G. Liu, X. Li, P. Ganesan, B.N. Popov, Appl. Catal. B: Environ. 93 (2009) 156.
[4] R. Borup, J. Meyers, B. Pivovar, Y.S. Kim, R. Mukundan, N. Garland, D. Myers, M. Wilson, F. Garzon, D. Wood, P. Zelenay, K. More, K. Stroh, T. Zawodzinski, J. Boncella, J.E. McGrath, M. Inaba, K. Miyatake, M. Hori, K. Ota, Z. Ogumi, S. Miyata, A. Nishikata, Z. Siroma, Y. Uchimoto, K. Yasuda, K.I. Kimijima, N. Iwashita, Chem. Rev. 107 (2007) 3904.
[5] H. Chang, S.H. Joo, C.H. Pak, J. Mater. Chem. 17 (2007) 3078.
[6] S.-H. Liu, J.-R. Wu, Int. J. Hydrogen Energy 36 (2011) 87.
[7] J.X. Wang, H. Inada, L. Wu, Y. Zhu, Y.M. Choi, P. Liu, W.P. Zhou, R.R. Adzic, J. Am. Chem. Soc. 131 (2009) 17298.
[8] S.G. Ramos, M.S. Moreno, G.A. Andreasen, W.E. Triaca, Int. J. Hydrogen Energy 35 (2010) 5925.
[9] E.B. Fox, H.R. Colon-Mercado, Int. J. Hydrogen Energy 35 (2010) 3280.
[10] R. Kobayashi, J. Ozaki, Catal. Lett. 28 (2009) 396.
[11] S. Kundu, T.C. Nagaiah, W. Xia, Y. Wang, S.V. Dommele, J.H. Bitter, M. Santa, G. Grundmeier, M. Bron, W. Schuhmann, M. Muhler, J. Phys. Chem. C 113 (2009) 14302.
[12] Y.G. Chen, J.J. Wang, H. Liu, R.Y. Li, X.L. Sun, S.Y. Ye, S. Knight, Electrochem. Commun. 11 (2009) 2071.
[13] C.G. Chung, L. Kim, Y.W. Sung, J. Lee, J.S. Chung, Int. J. Hydrogen Energy 34 (2009) 8974.
[14] G. Gupta, D.A. Slanac, P. Kumar, J.D. Wiggins-Camacho, J. Kim, R. Ryoo, K.J. Stevenson, K.P. Johnston, J. Phys. Chem. C 114 (2010) 10796.
[15] G. Liu, X. Li, P. Ganesan, B.N. Popov, Appl. Catal. B: Environ. 93 (2009) 156.
[16] Y.Y. Shao, J. Lin, Y. Wang, Y.H. Lin, J. Mater. Chem. 19 (2009) 46.
[17] M. Sakthivel, A. Schlange, U. Kunz, T. Turek, J. Power Sources 195 (2010) 7083.
[18] T. Iwazaki, H.S. Yang, R. Obinata, W. Sugimoto, Y. Takasu, J. Power Sources 195 (2010) 5840.
[19] H.J. Wang, L.A. Wang, Y. Nemoto, N. Suzuki, Y. Yamauchi, J. Nanosci. Nanotechnol. 10 (2010) 6489.
[20] Y.Y. Shao, S. Zhang, C.M. Wang, Z.M. Nie, J. Liu, Y. Wang, Y.H. Lin, J. Power Sources 195 (2010) 4600.
[21] X.Q. Wang, J.S. Lee, Q. Zhu, J. Liu, Y. Wang, S. Dai, Chem. Mater. 22 (2010) 2178.
[22] S. Pylypenko, T.S. Olson, N.J. Carroll, D.N. Petsev, P. Atanassov, J. Phys. Chem. C 114 (2010) 4200.
[23] S. Ghosh, C.R. Raj, J. Phys. Chem. C 114 (2010) 10843.
[24] V. Selvaraj, A. Nirmala Grace, M. Alagar, J. Colloid Interface Sci. 333 (2009) 254.

[25] S.H. Joo, S.J. Choi, I. Oh, J. Kwak, Z. Liu, O. Terasaki, R. Ryoo, Nature 412 (2001) 169.
[26] J. Ding, K.Y. Chan, J. Ren, F.S. Xiao, Electrochim. Acta 50 (2005) 3131.
[27] F. Su, J. Zeng, X. Bao, Y. Yu, J.Y. Lee, X.S. Zhao, Chem. Mater. 17 (2005) 3960.
[28] Y. Shimazaki, Y. Kobayashi, S. Yamada, T. Miwa, M. Konno, J. Colloid Interface Sci. 292 (2005) 122.
[29] F.J. Lai, H.L. Chou, L.S. Sarma, D.Y. Wang, Y.C. Lin, J.F. Lee, B.J. Hwang, C.C. Chen, Nanoscale 2 (2010) 573.
[30] M.B. Dawidziuk, F. Carrasco-Marin, C. Moreno-Castilla, Carbon 47 (2009) 2679.
[31] K.-W. Wang, C.-T. Yeh, J. Colloid Interface Sci. 325 (2008) 203.
[32] V. Lordi, N. Yao, J. Wei, Chem. Mater. 13 (2001) 733.
[33] Y.S. Gu, X.M. Hou, H.Y. Hu, B. Yu, L.X. Wang, F. Zhou, Mater. Chem. Phys. 116 (2009) 284.
[34] X.M. Hou, L.X. Wang, F. Zhou, F. Wang, Carbon 47 (2009) 1209.
[35] Z.C. Tang, D.S. Geng, G.X. Lu, J. Colloid Interface Sci. 287 (2005) 159.
[36] H.C. Tu, W.L. Wang, C.C. Wan, Y.Y. Wang, J. Phys. Chem. B 110 (2006) 15988.
[37] Z.F. Liu, E.T. Ada, M. Shamsuzzoha, G.B. Thompson, D.E. Nikles, Chem. Mater. 18 (2006) 4946.
[38] D.R.M. Godoi, J. Perez, H.M.K. Villullas, J. Electrochem. Soc. 154 (2007) B474.
[39] C. Park, I.Y. Jang, W. Wongwiriyapan, S. Morimoto, Y.J. Kim, Y.C. Jung, T. Toya, M. Endo, J. Mater. Chem. 20 (2010) 5345.
[40] J. Solla-Gullón, E. Gómez, E. Vallés, A. Aldaz, J.M. Feliu, J. Nanopart. Res. 12 (2010) 1149.
[41] D. Zhao, J. Feng, Q. Huo, N. Melosh, G.H. Fredrickson, B.F. Chmelka, G.D. Stucky, Science 279 (1998) 548.
[42] S.-H. Liu, R.-F. Lu, S.-J. Huang, A.-Y. Lo, S.-H. Chien, S.-B. Liu, Chem. Commun. 34 (2006) 3435.
[43] S.-H. Liu, W.-Y. Yu, C.-H. Chen, A.-Y. Lo, B.-J. Hwang, S.-H. Chien, S.-B. Liu, Chem. Mater. 20 (2008) 1622.
[44] S.-H. Liu, C.-C. Chiang, M.-T. Wu, S.-B. Liu, Int. J. Hydrogen Energy 35 (2010) 8149.
[45] L. Li, J.L. Shi, Nanotechnology 17 (2006) 344.
[46] L.X. Zhang, J.L. Shi, J. Yu, Z.L. Hua, X.G. Zhao, M.L. Ruan, Adv. Mater. 14 (2002) 1510.
[47] H. Parala, H. Winkler, M. Kolbe, A. Wohlfart, R.A. Fischer, R. Schmechel, H. von Seggern, Adv. Mater. 12 (2000) 1050.
[48] A.L. Patterson, Phys. Rev. 56 (1939) 978.
[49] S.H. Joo, K.J. Kwon, D.J. You, C.H. Pak, H. Chang, J.M. Kim, Electrochim. Acta 54 (2009) 5746.
[50] H. Darmstadt, C. Roy, S. Kaliaguine, S.J. Choi, R. Ryoo, Carbon 40 (2002) 2673.
[51] H. Darmstadt, C. Roy, S. Kaliaguine, T.W. Kim, R. Ryoo, Chem. Mater. 15 (2003) 3300.
[52] B. Sakintuna, Y. Yürüm, Ind. Eng. Chem. Res. 44 (2005) 2893.